Chinese Journal of Natural Medicines

Single-cell analysis reveals synergistic therapeutic mechanisms of Shenqi Fuzheng formula against acute myocardial infarction

Menglei Wang, Xiang Li, Meng Gao, Bingjie Zhu, Tiezhu Wei, Wenhua Huang, Xiaohui Fan, Jie Liao

Citation: Menglei Wang, Xiang Li, Meng Gao, Bingjie Zhu, Tiezhu Wei, Wenhua Huang, Xiaohui Fan, Jie Liao, Single-cell analysis reveals synergistic therapeutic mechanisms of Shenqi Fuzheng formula against acute myocardial infarction, Chinese Journal of Natural Medicines, 2026, 24(10), 1191-1204. doi: 10.1016/S1875-5364(26)61214-9.

View online: https://doi.org/10.1016/S1875-5364(26)61214-9

Related articles that may interest you

Chemical composition-based characterization of the anti-allergic effect of Guominkang Formula on IgE-mediated mast cells activation and passive cutaneous anaphylaxis

Chinese Journal of Natural Medicines. 2022, 20(12), 925-936 https://doi.org/10.1016/S1875-5364(22)60225-5

Gualou-Xiebai-Banxia decoction protects against type II diabetes with acute myocardial ischemia by attenuating oxidative stress and apoptosis *via* PI3K/Akt/eNOS signaling

Chinese Journal of Natural Medicines. 2021, 19(3), 161-169 https://doi.org/10.1016/S1875-5364(21)60017-1

Determining the protective effects of Ma-Mu-Ran Antidiarrheal Capsules against acute DSS-induced enteritis using 16S rRNA gene sequencing and fecal metabolomics

Chinese Journal of Natural Medicines. 2022, 20(5), 364-377 https://doi.org/10.1016/S1875-5364(22)60158-4

Transcriptome sequencing and metabolome analysis reveal the mechanism of Shuanghua Baihe Tablet in the treatment of oral mucositis

Chinese Journal of Natural Medicines. 2021, 19(12), 930-943 https://doi.org/10.1016/S1875-5364(22)60150-X

Fu-Zheng-Yi-Liu Formula inhibits the stem cells and metastasis of prostate cancer *via* tumor-associated macrophages/C-C motif chemokine ligand 5 pathway in tumor microenvironment

Chinese Journal of Natural Medicines. 2024, 22(6), 501-514 https://doi.org/10.1016/S1875-5364(24)60653-9

Er-xian ameliorates myocardial ischemia-reperfusion injury in rats through RISK pathway involving estrogen receptors

Chinese Journal of Natural Medicines. 2022, 20(12), 902-913 https://doi.org/10.1016/S1875-5364(22)60213-9

Wechat

Chinese Journal of Natural Medicines 24 (2026) 1191-1204

Contents lists available at ScienceDirect

Chinese Journal of Natural Medicines

journal homepage: www.cjnmcpu.com/

Original article

Single-cell analysis reveals synergistic therapeutic mechanisms of Shenqi Fuzheng formula against acute myocardial infarction

Menglei Wang[a,b,Δ], Xiang Li[a,c,Δ], Meng Gao[a,b], Bingjie Zhu[a,b], Tiezhu Wei[a,c], Wenhua Huang[d], Xiaohui Fan[a,b,e,f,*], Jie Liao[a,b,e,f,*]

[a] *State Key Laboratory of Chinese Medicine Modernization, School of Pharmacy, Zhejiang University, Hangzhou 310058, China*
[b] *Zhejiang Key Laboratory of Chinese Medicine Modernization, Innovation Center of Yangtze River Delta, Zhejiang University, Jiaxing 314100, China*
[c] *School of Basic Medical Sciences and Forensic Medicine, Hangzhou Medical College, Hangzhou 310063, China*
[d] *Limin Pharmaceutical Factory, Livzon Pharmaceutical Group Inc., Shaoguan 512028, China*
[e] *International Science and Technology Cooperation Base of Chinese Medicine Modernization and Big Health, Innovation Center of Yangtze River Delta, Zhejiang University, Jiaxing 314102, China*
[f] *Hangzhou TCM Hospital Affiliated to Zhejiang Chinese Medical University, Hangzhou 310007, China*

ARTICLE INFO

Article history:
Received 3 February 2026
Revised 26 July 2026
Accepted 28 July 2026
Available online 20 October 2026

Keywords:
Shenqi Fuzheng formula
Efficacy enhancement
Synergistic mechanism
Acute myocardial infarction
Chemical composition
Single-cell RNA sequencing

ABSTRACT

The Shenqi Fuzheng (SQ) formula, made from Codonopsis Radix (*Dangshen*, DS) and Astragali Radix (*Huangqi*, HQ), has been used in Traditional Chinese Medicine (TCM) and exhibits cardio-protective effects against acute myocardial infarction (AMI). However, the molecular basis of DS-HQ synergy remains unclear. Here, we combined RNA sequencing (RNA-seq) and single-cell RNA sequencing (scRNA-seq) to explore their synergistic mechanisms. Transcriptomic analyses showed that SQ influenced the AMI network more effectively than either herb alone. ScRNA-seq analysis revealed that these synergistic effects involve both direct and indirect pro-angiogenic pathways. The combination treatment enhanced pro-angiogenic responses in microvascular endothelial subpopulations and promoted angiogenesis in the border zone. It also enhanced the anti-inflammatory role of a specific reparative macrophage subset and stimulated vascular endothelial growth factor A (VEGFA) secretion from these cells, supporting the VEGFA-VEGFR signaling between macrophages and microvascular endothelial cells. This coordinated regulation provides a plausible mechanistic explanation for the reduced infarct size and improved cardiac outcomes seen *in vivo*, highlighting the therapeutic value of TCM.

1. Introduction

The Shenqi Fuzheng (SQ) formula is a classic herbal combination in Traditional Chinese Medicine (TCM), prepared from Codonopsis Radix (*Dangshen*, DS) and Astragali Radix (*Huangqi*, HQ) [1]. Guided by TCM theory, it is traditionally used to supplement qi and strengthen vital *qi* (Yiqi Fuzheng) [2]. Clinically, SQ has long been used with well-documented effects on immune function and fatigue-related symptoms, particularly as an adjuvant therapy for patients with cancer undergoing chemotherapy or radiotherapy [3-5]. Owing to its long clinical history and extensive application, SQ has been recognized as a well-tolerated formulation, with a favorable safety profile established through decades of clinical use. This long-standing record of safety and efficacy provides a solid foundation for broader therapeutic exploration beyond oncology research.

Recent clinical studies have demonstrated its beneficial effects in cardiovascular diseases, including improved cardiac function and enhanced myocardial performance in patients with heart failure after acute myocardial infarction (AMI) [6, 7]. Furthermore, it can significantly reduce peripheral blood levels of angiotensin II (Ang II) and endothelin-1 (ET-1), improving therapeutic efficacy in patients with chronic heart failure [8]. When administered in combination with conventional therapy, it has also been shown to markedly decrease plasma B-type natriuretic peptide (BNP) concentrations, enhance ventricular function, and potentiate treatment outcomes [9].

AMI is characterized by multifaceted pathological processes rather than a single pathological mechanism and is a leading cause of mortality worldwide [10, 11]. Coronary artery occlusion triggers a cascade of events, including myocardial injury that exacerbates oxidative stress, excessive inflammatory responses, massive cardiomyocyte apoptosis, impaired vascular endothelial function, and myocardial fibrosis [12, 13]. Despite advances in revascularization strategies (e.g., percutaneous coronary intervention, PCI) [14, 15] and the use of single-target drugs such as β-blockers and ACE inhibitors, these interventions primarily address specific aspects of AMI pathophysiology and may not adequately modulate the complex interplay among multiple pathological pathways [16]. Therefore, post-AMI heart failure and mortality rates remain elevated, highlighting the urgent need for therapies that are capable of simultaneously modulating multiple pathological tar-

* Corresponding author.
E-mail addresses: fanxh@zju.edu.cn (X. Fan); liaojie@zju.edu.cn (J. Liao)
Δ These authors contributed equally to this work.

https://doi.org/10.1016/S1875-5364(26)61214-9
Copyright © 2026, China Pharmaceutical University. Published by Elsevier B.V. All rights are reserved.

gets.

The SQ formula, with its complex chemical composition, inherently possesses a "multi-component, multi-target, and multi-pathway" potential, aligning well with the complex pathological features of AMI. Our previous studies have demonstrated that SQ protects against myocardial ischemia-reperfusion (IR) injury in rats, reducing infarct size and attenuating apoptosis and inflammation [2]. However, these findings were limited in two key respects: first, the effects of SQ were not compared with those of its individual components (DS and HQ), leaving the rationale for combining the two herbs and their potential synergistic effects unexplored; second, the analyses were based on microarray, which masks cell-type-specific responses and fails to reveal key subpopulations driving the protective effects of SQ.

To address these gaps, we first investigated whether DS and HQ exert synergistic cardioprotective effects in AMI, and subsequently sought to identify the molecular programs and cellular populations potentially underlying the observed therapeutic synergy. Therefore, we adopted a comprehensive approach, in which the cardioprotective effects of SQ, DS, and HQ in AMI rats were studied to evaluate potential synergy. RNA sequencing (RNA-seq) and network pharmacology were performed to identify key targets and differentially expressed genes (DEGs) in AMI and TCM treatment. Based on these targets, single-cell RNA sequencing (scRNA-seq) of non-cardiomyocytes from treated rat myocardial tissue was conducted to map cell-type-specific transcriptional changes induced by SQ versus single herbs and to pinpoint key regulated cell subpopulations, providing insights into cell state transitions and cell-cell interactions (CCI) within the microenvironment [17]. This integrated approach provides a more comprehensive mechanistic framework for SQ, offering new insights into the modernization of TCM compound research.

2. Materials and methods

2.1. Preparation of TCM extracts

DS and HQ were prepared from Codonopsis Radix (dried root of *Codonopsis pilosula*) and Astragali Radix (dried root of *Astragalus membranaceus*), respectively. The combined extract, designated SQ, was prepared by co-extracting Codonopsis Radix and Astragali Radix at a 1:1 ratio. Each component was extracted and concentrated. Ethanol was used during the extraction process to improve the extraction efficiency of bioactive constituents with moderate polarity, reduce insoluble impurities, and enhance the consistency and stability of the extracts. High-performance liquid chromatography (HPLC) analysis of the extracts was conducted according to previously published methods [2].

2.2. Chromatographic experiments, mass spectrometry, and chemical composition identification

The extract was centrifuged at 10 000 r·min^{-1} for 10 min, and the supernatant was reserved. Chromatographic separation was performed using an ACQUITY UPLC HSS T3 column (2.1 × 150 mm, 1.8 μm; Waters, MA, USA). Data were acquired using an ACQUITY UPLC system (Waters, MA, USA) coupled to a TripleTOF 6600+ quadrupole time-of-flight mass spectrometer (SCIEX, MA, USA). The detection conditions were consistent with those of the previous study on the SQ formula [1].

Mass measurements were performed in negative and positive ion modes. The detection conditions were consistent with previous studies [1]. Mass axis error (< 2 × 10^{-6}) was ensured before injection.

Raw mass data were imported into MS-DIAL software (v 4.9). All settings were kept at the default. The resulting peak list was exported for component identification.

2.3. Animal model and drug administration

Male Sprague Dawley (SD) rats (220–250 g) were provided by Shanghai SLAC Laboratory Animal Co., Ltd. (Shanghai, China, SCXK (Shanghai) 2022-0004). The rats were raised under a 12-h light/dark cycle. Food and water were provided ad libitum. The Animal Care and Use Committee of the Zhejiang University School of Medicine approved the animal experiments (Protocol Number: ZJU20250197).

After transportation, all rats experienced a standardized acclimation period under normal housing conditions and were randomly assigned to experimental groups before any intervention. The rats were assigned into different groups, namely Sham, Model, HQ-low (HQ-L, 4 g crude drug·kg^{-1}), HQ-high (HQ-H, 8 g crude drug·kg^{-1}), DS-low (DS-L, 4 g crude drug·kg^{-1}), DS-high (DS-H, 8 g crude drug·kg^{-1}), SQ-low (SQ-L, 8 g crude drug·kg^{-1}), and SQ-high (SQ-H, 16 g crude drug·kg^{-1}). The gavage dose in the SQ-H group was eight times the clinical intravenous equivalent dose to compensate for the lower bioavailability of oral administration [2]. SQ contains multiple components with different pharmacokinetic properties. Therefore, we based the calculation on Astragaloside IV (the main quality control index of Astragali Radix in the *Chinese Pharmacopeia*). The oral bioavailability of Astragaloside IV is relatively low (about 2%–4%) [18, 19], and theoretically, the corresponding oral dose should be about 25 times higher than the equivalent intravenous dose. However, considering both efficacy and safety, we moderately reduced the dose to 8 times. For rats receiving vascular endothelial growth factor receptor (VEGFR) inhibitor, in addition to the above high-dose drug treatment, an additional 30 mg·kg^{-1} of Lenvatinib (MCE, HY-10981, USA) was administered [20]. The rats received oral gavage for 7 consecutive days as a preventive administration to establish a pharmacological background at the onset of ischemic injury. On the 8th day, after being anesthetized with 1.25% tribromoethanol, they underwent surgery to establish an AMI model through left anterior descending (LAD) artery ligation. After surgery, the rats received therapeutic drug administration for 3 days and were sacrificed on the 11th day. All efforts were made to minimize their suffering.

2.4. Preparation of drug-containing serum

Rats were continuously administered the doses described above for 7 days. Two hours after the last gavage, the rats were anaesthetized, and blood was collected from the abdominal aorta. The serum was centrifuged (4 °C, 3000 r·min^{-1}, 20 min), inactivated (56 °C, 30 min), filtered, and stored at −80 °C.

2.5. Echocardiography

Transthoracic echocardiography was performed to evaluate cardiac function and ventricular dimensions in rat hearts using the ultrasound system (Vinno Technology Ltd., Suzhou, China). Measurements were conducted 3 days after AMI. Rats were anesthetized *via* isoflurane inhalation (1.5%–2%) to ensure stability during the procedure. Echocardiographic imaging was acquired at the papillary muscle level using both two-dimensional (2D) and M-mode modalities. Left ventricular ejection fraction (LVEF) and left ventricular fractional shortening (LVFS) were calculated using the ultrasound system. Six rats were used for echocardiography measurement in each group.

2.6. Histopathological and immunofluorescence analysis

Histopathological and immunofluorescence analyses were

performed on three rats from each group. The heart tissue was first thoroughly rinsed with a 0.9% NaCl solution. It was then fixed in 4% paraformaldehyde solution (Servicebio, G1101, China), embedded in paraffin, and sectioned into 10 μm-thick slices. In histopathological analysis, the tissue sections were stained with hematoxylin and eosin (H&E), then dehydrated and sealed. The prepared sections were examined under an optical microscope (Olympus IX53, Tokyo, Japan), and representative images were captured for analysis. In immunofluorescence analysis, fixation, tissue processing, antigen retrieval, and blocking of nonspecific staining were performed on sections. Samples were incubated with the primary antibody at 4 °C overnight. Then, sections were incubated with the secondary antibodies, followed by counterstaining with DAPI. Samples were examined under a fluorescence microscope (3DHISTECH, Budapest, Hungary). The following primary antibodies were used: anti-CD31 (Servicebio, GB120008, China), anti-CD68 (Haoke, B03014R, China), anti-TREM2 (Biorbyt, orb668484, UK), and anti-VEGFA (Affinity, AF5131, China).

Immunofluorescence images from the border zone were analyzed by randomly selecting 5–7 areas, each with an approximate area of 130 000 μm^2. The number of microvessels, as well as the co-localization of CD68, TREM2, and VEGFA staining fluorescence with the cell nuclei (DAPI staining), were quantified in each selected region. The counting results were then summarized and plotted for further analysis.

2.7. Determination of myocardial infarct size

Myocardial infarct size was analyzed in six rats per group. The hearts were flushed with a 0.9% NaCl solution and quickly frozen at −20 °C. The area below the cardiac ligature was serially sectioned into five transverse slices (2 mm thick each), and the slices were incubated in TTC solution (Solarbio, G3004, China) at 37 °C for 10 min. Quantitative image analysis was performed to calculate the ratio of infarct size to the total area, evaluating the extent of myocardial infarction.

2.8. Combination index (CI) calculation

CI was calculated using the Bliss independence model [21]. The Sham group was assigned as representing a 100% treatment effect relative to the Model group. Meanwhile, the effects of treatment groups were expressed as percentages relative to the Sham group. The expected additive effect was determined using Eq. (1). When the CI value (Eq. (2)) was less than 1, it indicated a synergistic effect.

$$E_{DS+HQ} = E_{DS} + E_{HQ} - E_{DS}E_{HQ}\,(0 \leqslant E \leqslant 1) \tag{1}$$

$$\mathrm{CI} = \frac{E_{DS+HQ}}{E_{SQ}} \tag{2}$$

To verify the robustness of the synergy assessment, the Highest Single Agent (HSA) model [22] was also applied. In the HSA model, the expected effect of the combination was defined as Eq. (3). When the CI value (Eq. (4)) was less than 1, it indicated a synergistic effect.

$$E_{DS+HQ} = \max\left(E_{DS}, E_{HQ}\right)(0 \leqslant E \leqslant 1) \tag{3}$$

$$\mathrm{CI} = \frac{E_{DS+HQ}}{E_{SQ}} \tag{4}$$

2.9. RNA-seq

Three cardiac tissue samples (border zone regions) from rats in the Sham, Model, HQ-H, DS-H, and SQ-H groups were randomly selected for RNA-seq. Total RNA was extracted from cardiac tissue using TRIzol reagent (Invitrogen, 15596026, USA). RNA purity and quality were assessed, and the cDNA library was constructed with the Illumina NEBNext® Ultra™ RNA library prep kit (NEB, E7530, USA). Sequencing was conducted on the Illumina NovaSeq X Plus platform (Novogene, Beijing, China), and fragments were converted into sequence data (reads) using CASAVA. Alignment of reads to the reference genome was performed using Hisat2 (v2.0.5). DEGs between the two groups were analyzed. *P* value (adjusted) and Fold Change (Eq. (5)) were calculated by DESeq2.

$$\text{Fold change} = log_2E_{group1} - log_2E_{group2} \tag{5}$$

2.10. Construction of the AMI disease network

AMI shares fundamental pathological mechanisms with broader cardiovascular diseases (CVDs); therefore, CVD-associated genes were used as the disease knowledge framework to capture a broader range of disease-associated transcriptional changes. To ensure disease specificity, the AMI disease network was constructed by intersecting DEGs derived from the transcriptomic dataset with CVD-related genes (http://tcm.zju.edu.cn/chd/) [23]. The resulting network was visualized using Cytoscape (v3.10.0) and STRING (https://string-db.org/). The effects of DS, HQ, and SQ on the AMI network were evaluated using the Efficiency of Recovery Regulation (EoR; Eq. (6)) and a Network Topology and Transcriptomics-Based Approach (NTRA; Eq. (7-9)), as described in previous studies [2, 24, 25]. The EoR represented the restoration of each gene expression within the AMI network following treatment, with 100% representing complete restoration. The NTRA ranking method identified key genes within the AMI disease network and the pharmaceutical effect network.

$$\mathrm{EOR} = 100\% - \left|100\% - \frac{FoldChange\left(\frac{Drug}{Model}\right)}{FoldChange\left(\frac{Sham}{Model}\right)}\right| \tag{6}$$

$$\mathrm{Rank} = \mathrm{Rank}\,(\mathrm{RankT} + \mathrm{RankR}) \tag{7}$$

$$\mathrm{RankT} = \mathrm{Rank}\,(\mathrm{RankD} + \mathrm{RankB}) \tag{8}$$

$$\mathrm{RankR} = \mathrm{Rank}\,(\mathrm{RankF} + \mathrm{RankP}) \tag{9}$$

2.11. Real-time quantitative reverse transcription polymerase chain reaction assay (RT-qPCR)

For tissue samples, total RNA of Sham, Model, HQ-H, DS-H, and SQ-H groups was extracted from cardiac tissue using TRIzol reagent (Invitrogen, 15596026, USA). For cell samples, RNA was extracted from cells using the RNA-Quick purification kit (ES Science, RN001, China). RNA concentrations were determined, and all samples were diluted to the same concentration with RNase-free water (Beyotime, R0021, China). RNA samples were reverse transcribed using a HiFiScript cDNA synthesis kit (CoWin, CW2569M, China). Quantification of gene expression was carried out using the Hieff UNICON® universal blue qPCR SYBR green master mix (Yeasen, 11184ES08, China) and specific primers (Sangon, Shanghai, China) on the Bio-Rad CFX96 Touch™ system (Bio-Rad, CA, USA). Primer sequences are provided in Table S3. Relative gene expression was calculated using the $2^{-\Delta\Delta Ct}$, with *Gapdh* as the internal control.

2.12. Tissue collection and non-cardiomyocyte cell isolation

Cardiac tissues from three rats within each experimental group (Sham, Model, HQ-H, DS-H, and SQ-H) were pooled for scRNA-seq library preparation. Cardiac tissue samples were col-

lected from AMI or treated animal hearts, along with the corresponding regions from Sham hearts. The tissues were minced into small fragments and enzymatically digested. Then, the resulting cell suspensions were filtered through a 40-μm cell strainer to reduce the presence of large cardiomyocytes and enrich non-cardiomyocyte populations for downstream single-cell analysis. Red blood cells were lysed using red blood cell lysis buffer (MACS, 130-094-183, Germany) to ensure a clean and viable cell population for downstream analysis.

2.13. ScRNA-seq library construction

The single-cell library was prepared with the droplet-based 10 × Genomics Chromium System and Single Cell 3′ Reagent Kit v3 (10 × Genomics) according to the manufacturer's protocol. In brief, the remaining cells were partitioned into gel beads in emulsion (GEMs), where cell lysis and barcoded reverse transcription of RNA were conducted. cDNA was synthesized and amplified. Then, cDNA was fragmented, ligated with the adapter and sample index, and selected with SPRIselect Reagent Kit (Beckman, B23318, USA). The constructed library was sequenced on the NovaSeq 6000 Illumina sequencing platform.

2.14. Pre-analysis of single-cell expression

We processed the 10 × raw sequencing data using the Cell Ranger (10 × Genomics, v 8.0.1) suite. The reads were mapped using the CellRanger with a rat genome reference (mRatBn7). Table S4 summarizes the mapping results of the AMI dataset for each group. Raw gene expression matrices were filtered using the Seurat R package (v 5.0.3) [26], retaining cells with 300 to 7000 detected genes and less than 10% mitochondrial reads. The retained 55 839 cells were normalized with the default global scaling method. Highly variable genes were identified with the FindVariableFeatures function and expression values were scaled with the ScaleData function. Principal component analysis (PCA) was used for dimensionality reduction. Harmony was used to integrate samples. Cells were clustered by the FindClusters function. Visualization was realized with uniform manifold approximation and projection (UMAP) [27].

2.15. Cell-cell communication

The expression matrix was imported into CellChat [28] (v 2.1.2) for analysis. In the results of CellChat, the ligand-receptor pairs and interactions with a *P*-value < 0.05 were retained.

2.16. Gene Ontology (GO) enrichment

When analyzing RNA-seq data, analysis was performed on genes with synergistic effects using Metascape (https://metascape.org/gp/index.html). In scRNA-seq data, a subset of DEGs was identified with the FindAllMarkers function. For downstream analyses, the DEGs were filtered by the following settings (logfc. threshold = 0.5, only. pos = T), and the DEGs with an adjusted *P*-value (Wilcoxon test) < 0.05 were retained. To perform GO enrichment analysis, the top 100 DEGs ranked by fold change were selected and analyzed using Metascape. Enrichment results were filtered using a threshold (*P*-value < 0.01). Biological Processes (BP) terms were retained.

2.17. Scoring of BP

The scores of cells were defined as the average standardized expression value of gene signatures representing distinct biological functions. The score for "Angiogenesis" was calculated based on DEGs associated with the angiogenesis pathway.

2.18. Cell culture and viability assay

HUVECs were obtained from the Chinese Academy of Sciences Cell Bank. HUVECs were cultured in low-glucose DMEM (Gibco, C11885500BT, USA) with 10% fetal bovine serum (FBS, Gibco, A5669701, USA) and 1% penicillin/streptomycin (P/S, Gibco, 15140-122, USA) in a humidified incubator with 5% CO_2 at 37 °C. The cytotoxicity of different drug concentrations was evaluated in HUVECs to determine the optimal dose. The viability of HUVECs was assessed using the Cell Counting Kit-8 (CCK-8) assay (Yeasen, 40203ES60, China) according to the manufacturer's protocol. Absorbance was measured with a spark multimode microplate reader (Tecan, Mannedorf, Switzerland) at 450 nm. HUVECs were treated with 10% drug-containing serum (Fig. S6).

2.19. Wound healing assay

When HUVECs reached 80%–90% confluence in 12-well plates, a scratch was made using a pipette tip. The initial scratch width was recorded after washing thrice with DMEM. The culture medium was then replaced with DMEM containing 1% P/S and one of the following treatments: (i) blank serum (control group), (ii) drug-containing serum, or (iii) blank serum supplemented with 20 ng·mL^{-1} VEGFA (TargetMol Chemicals, TMPK-00823, USA) as a positive control. Scratch width was recorded after 12 h of treatment. The degree of scratch healing was observed with the optical microscope (Olympus IX53, Tokyo, Japan).

2.20. Bone marrow-derived macrophages (BMDMs) extraction

Tibiae and femurs from 10-day-old SD rats (Shanghai SLAC Laboratory Animal Co., Ltd.) were sterilized in 75% ethanol for 3–5 min. Bone marrow was flushed with high-glucose DMEM (10% FBS, 1% P/S), filtered through a 70-μm strainer, and centrifuged (500 g, 10 min, 4 °C). 5 mL erythrocyte lysis solution (Beyotime, C3702, China) was added, and the cells were incubated at 4 °C for 5 min. The solution was centrifuged at 1000 r·min^{-1} for 3 min. The cells were resuspended in complete DMEM and inoculated into 10-cm culture dishes. After 2 h, the supernatant was centrifuged (1000 r·min^{-1}, 3 min, 4 °C). The cells were resuspended in DMEM with 10% FBS, 1% P/S, and 10 ng·mL^{-1} M-CSF (MCE, HY-P7247, USA), then inoculated at a density of 1 × 10^6 cells·mL^{-1} in culture plates. Half of the liquid volume was renewed after 2 days. The CCK-8 assay was used to assess the optimal treatment concentration in BMDMs. BMDMs were treated with 10% drug-containing serum (Fig. S8).

The study included five experimental groups: CON, Model, DS, HQ, and SQ groups. BMDMs in the Model group were stimulated with 100 ng·mL^{-1} LPS (Solarbio, L8880, China) and 20 ng·mL^{-1} IFN-γ (MCE, HY-P7095, USA) for 24 h. The drug-treated groups underwent the same stimulation protocol and drug-containing serum treatments.

2.21. Detection of nitric oxide (NO) production

BMDMs were cultured to 80% confluence. After different treatments, the cell supernatants were extracted and assayed using the NO assay kit (Beyotime, S0021, China). After adding the samples, Griess reagent I and Griess reagent II, the NO concentration was measured at 540 nm using the spark multimode microplate reader.

2.22. Vascular endothelial growth factor A (VEGFA) detection

BMDMs were cultured to 80% confluence. After different

treatments, the cell supernatant was collected and assayed using the VEGFA ELISA kit (USCN, USEA143Ra, China). VEGFA concentration was measured at 450 nm using the Spark multimode microplate reader.

2.23. Molecular docking

VEGFA was selected as the receptor, with the drug components serving as ligands. The 3D structure of VEGFA was obtained from the PDB database (https://www.rcsb.org/) and preprocessed using PyMOL software (v 3.1.0). The 3D structures of the drug components were retrieved in Mol2 format from the TCMSP database (https://www.tcmsp-e.com/). Molecular docking simulations between VEGFA and the drug components were performed using AutoDock Vina (v 1.1.2). The conformation exhibiting the lowest binding energy was selected for further analysis, and the results were visualized using PyMOL.

2.24. Statistical analysis

Data presented as mean ± standard error of the mean (SEM) were analyzed using GraphPad Prism (v 9.0.0). One-way analysis of variance (ANOVA) was used for multiple group comparisons. When comparisons were performed among all groups, Tukey's multiple comparisons test was applied. When comparisons were made against a single control, Dunnett's post hoc test was used. $P < 0.05$ was defined as statistically significant.

3. Results

3.1. Significant differences in chemical composition were observed between DS and HQ

To identify potential active constituents in SQ, DS, and HQ were analyzed using UPLC-Triple-TOF/MS, which yielded both positive and negative total ion chromatograms (Figs. 1A–1D). A total of 24 compounds were identified in DS and 55 in HQ (Tables. S1–S2). DS is mainly composed of alkaloids (e.g., codonopsine), alkyl polyglucosides (e.g., lobetyolin), phenylpropanoids, and other constituents. HQ primarily contains flavonoids (e.g., calycosin 7-*O*-glucopyranoside), terpenoids (e.g., astragaloside IV), and related compounds (Figs. 1E and 1F).

3.2. SQ (DS and HQ) exhibits synergistic efficacy compared with DS or HQ monotherapy

To evaluate the therapeutic effects of DS, HQ, and SQ on AMI, we established an AMI rat model by continuously administering low or high doses of extracts for 7 d, with treatment continuing

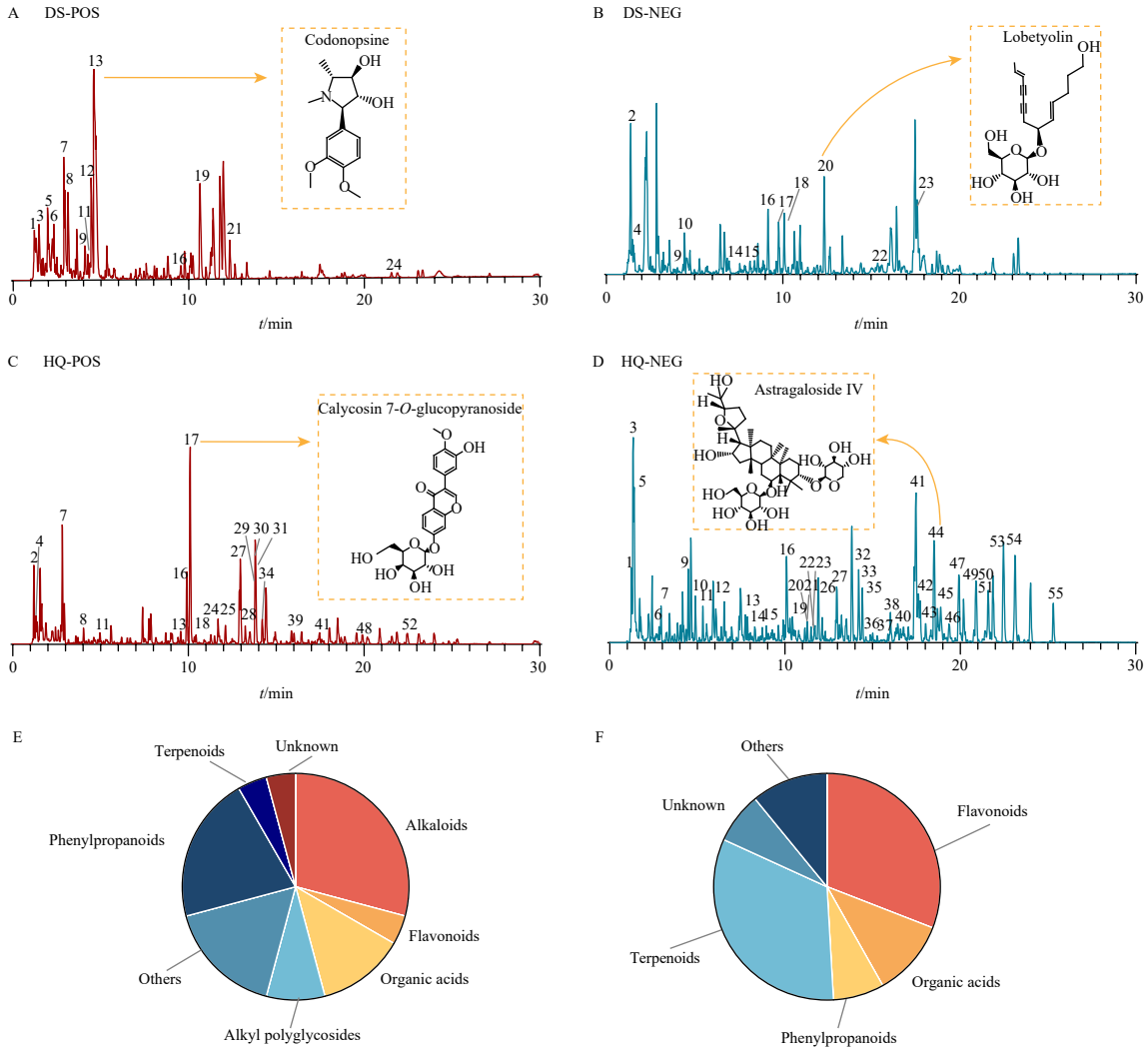


Fig. 1 Chemical composition of DS and HQ. (A) TIC of DS by UPLC-Triple-TOF/MS, positive ion mode. (B) TIC of DS by UPLC-Triple-TOF/MS, negative ion mode. (C) TIC of HQ by UPLC-Triple-TOF/MS, positive ion mode. (D) TIC of HQ by UPLC-Triple-TOF/MS, negative ion mode. (E) Pie chart of the percentage of compound types in DS. (F) Pie chart of the percentage of compound types in HQ. TIC, total ion current chromatograms; DS, Codonopsis Radix extract; HQ, Astragali Radix extract.

for 3 d after surgery (Fig. 2A). H&E staining showed that the combination therapy reduced myocardial damage more effectively than DS or HQ alone (Fig. 2B). The myocardial infarct size was measured using TTC staining. The average infarct area ratio was reduced in the DS and HQ groups compared with the Model group, and was further decreased in the SQ group (Figs. 2C–2D, Fig. S1A). CI analysis indicated a synergistic interaction between DS and HQ in reducing infarct size (Fig. 2E, Fig. S1B). To evaluate cardiac function, we analyzed the key echocardiographic parameters (Fig. 2F). The LVEF and LVFS were significantly decreased after AMI. DS or HQ treatment significantly improved cardiac function compared with the Model group, whereas the SQ extract showed a more pronounced effect than either DS or HQ alone (Figs. 2G–2H). CI analysis further supported a synergistic interaction between DS and HQ in improving cardiac function (Figs. 2I–2J, Figs. S1C-S1D).

3.3. Integrated RNA-seq and single-cell analyses identify molecular and cellular responses associated with combination treatment in AMI

Having established the synergistic cardioprotective effects of DS and HQ *in vivo*, we next sought to identify the molecular programs and cellular populations potentially underlying this therapeutic synergy. To elucidate the mechanism underlying the effects of the combination of DS and HQ against AMI, we employed RNA-seq and network pharmacology to construct an AMI disease network. Comparing 1524 protein-coding genes related to

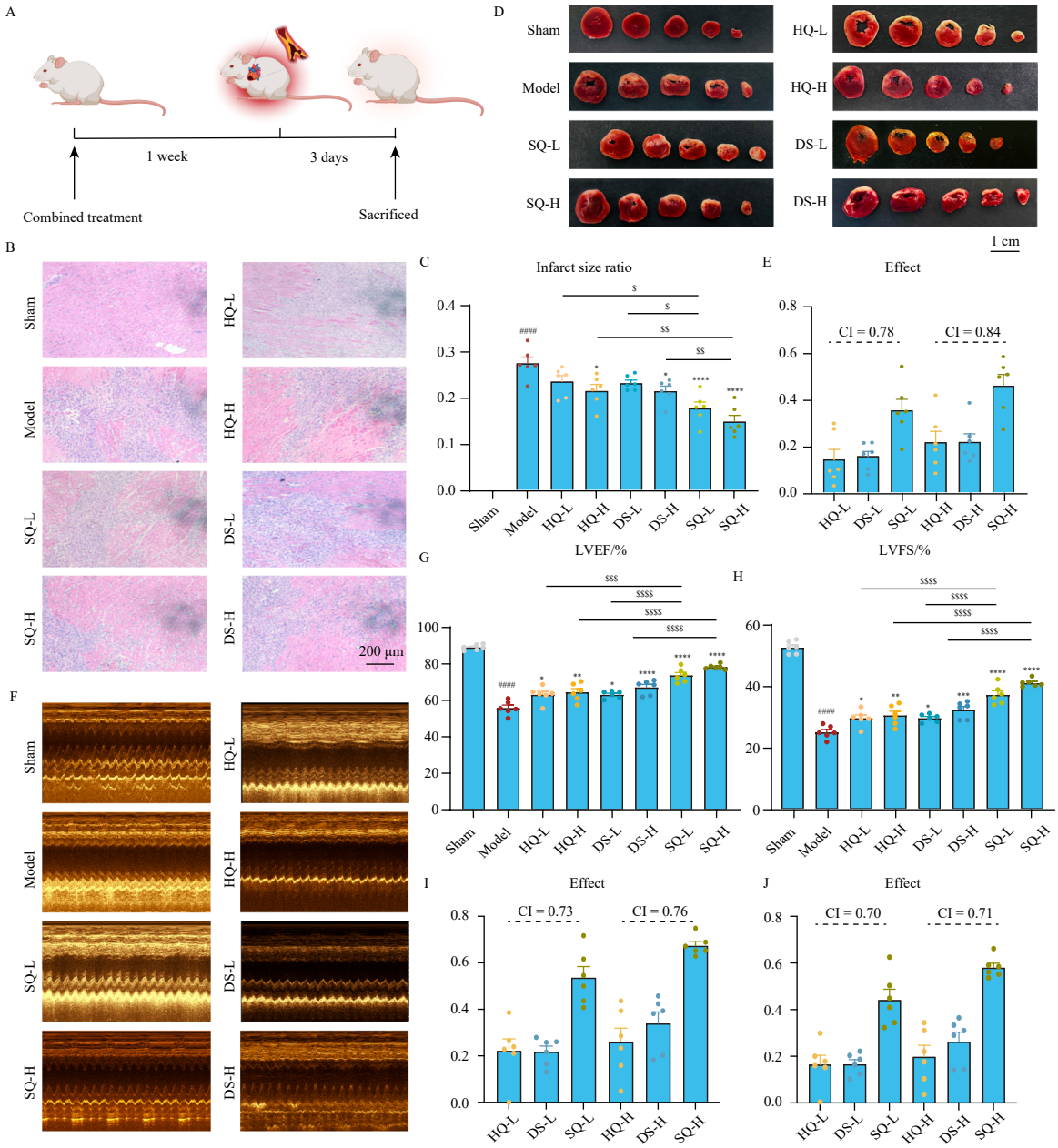


Fig. 2 DS combined with HQ effectively reduces infarct size and injury to the heart. (A) Overview of the experimental processes. (B) H&E staining of cardiac sections in AMI rats after treatment with DS, HQ, and SQ extracts, $n = 3$. (C) Infarct size ratio of the heart in AMI rats after treatment with DS, HQ, and SQ extracts, $n = 6$. (D) Representative image of TTC staining. (E) CI calculation of infarct size ratio in AMI rats after treatment with DS, HQ, and SQ extracts, $n = 6$. (F) M-mode echocardiograms 3 d after AMI. (G) The LVEF in AMI rats after treatment with DS, HQ, and SQ extracts, $n = 6$. (H) The LVFS in AMI rats after treatment with DS, HQ, and SQ extracts, $n = 6$. (I) CI calculation of LVEF in AMI rats after treatment with DS, HQ, and SQ extracts, $n = 6$. (J) CI calculation of LVFS in AMI rats after treatment with DS, HQ, and SQ extracts, $n = 6$. Data are presented as mean ± SEM. $^{\#\#\#\#}P < 0.0001$ *vs* the Sham group; $^{*}P < 0.05$, $^{**}P < 0.01$, $^{***}P < 0.001$, $^{****}P < 0.0001$ *vs* the Model group; $^{\$}P < 0.05$, $^{\$\$}P < 0.01$, $^{\$\$\$}P < 0.001$, $^{\$\$\$\$}P < 0.0001$ *vs* the SQ-L or SQ-H group. CI, combination index; L, low-dose group; H, high-dose group; DS, Codonopsis Radix extract; HQ, Astragali Radix extract; SQ, Shenqi Fuzheng extract.

CVDs [23] with genes obtained through RNA-seq data, we identified 1376 overlapping genes. Furthermore, utilizing protein-protein interaction (PPI) data from the STRING database, we constructed an AMI network comprising 1346 nodes and 39 333 interactions (Fig. 3A). The EoR was used to quantify the impact of drugs on disease-related genes. SQ restored the expression of 77.49% (1043 out of 1346) of the dysregulated genes, DS regulated 43.91% (591 out of 1346) of the genes, and HQ regulated 49.26% (663 out of 1346) of the genes. These results indicate a broader restoration of AMI-associated transcriptional dysregulation by the combination treatment than by either monotherapy.

Genes showing an EoR value exceeding 0.2 under combination treatment relative to monotherapy were considered to exhibit combination-enhanced regulation and were included in subsequent analyses. The pathways enriched in these genes were strongly associated with AMI (Fig. 3B, S2A). DS and HQ co-regulated some molecular targets (Fig. 3C). For example, *Edn1*, *Enpp1*, *Acp5*, *Ghr*, *F3*, *Prkce*, and *Vegfr1* have been implicated in oxidat-

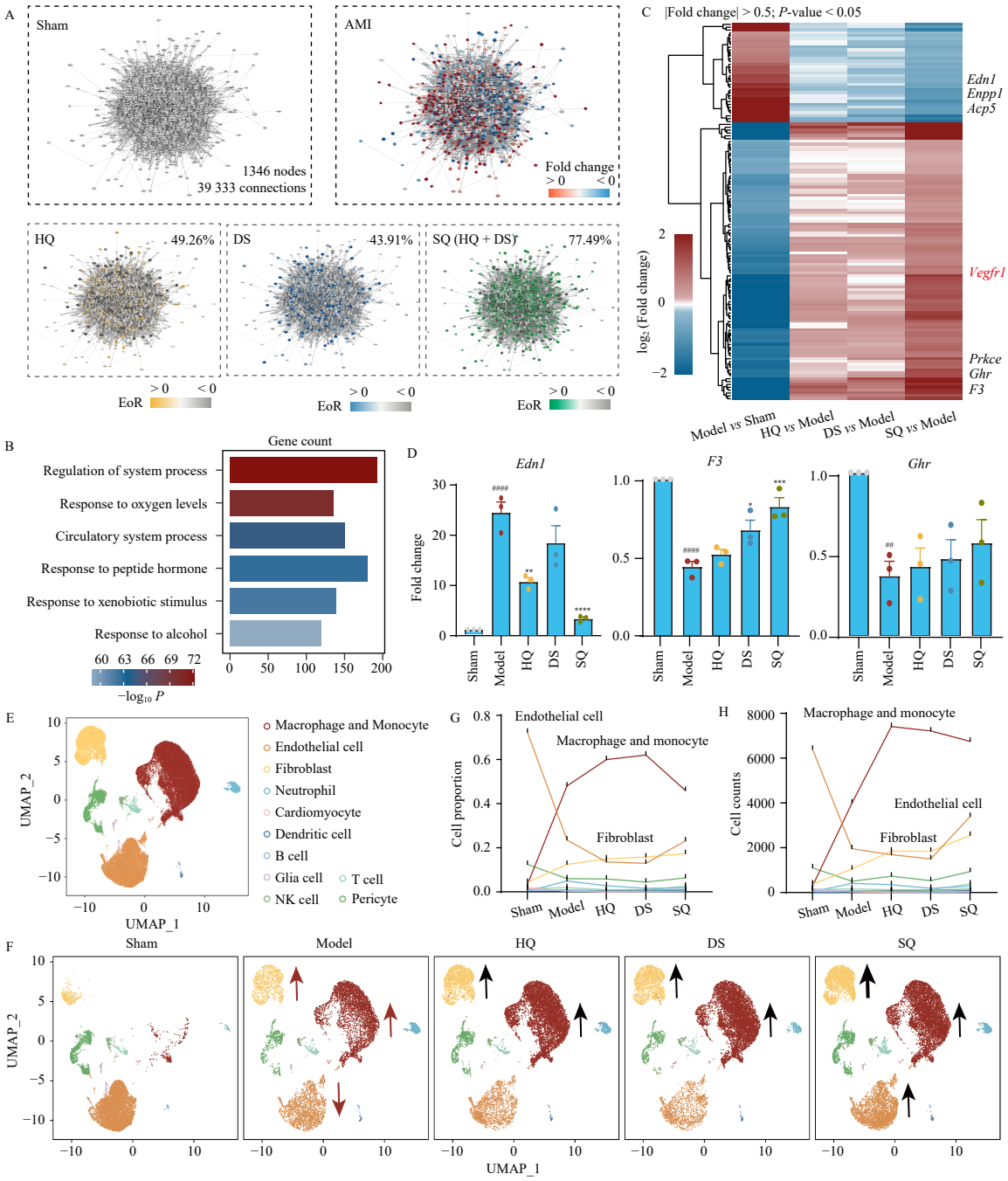


Fig. 3 Effect of the combination of DS and HQ on AMI networks and cell populations. (A) Network of each group. Top left, Sham group. The node size represents the NTRA ranking; the higher the ranking, the larger the node size. Top right, Model group. Blue represents downregulated gene expression in AMI, and red indicates upregulated gene expression in AMI. Bottom, treatment groups. The yellow, blue, and green colors indicate the degree of gene recovery regulation after drug treatment; the black color represents no recovery regulation of the gene. (B) The top six pathways were obtained from GO enrichment. (C) The heatmap of the expression patterns of co-regulated DEGs (Model *vs* Sham: |Fold change| > 0.5; *P*-value < 0.05). (D) The gene expression levels of *Edn1*, *F3*, and *Ghr* were identified using RT-qPCR. *Gapdh* is the internal reference, n = 3. Data are presented as mean ± SEM. $^{\#\#}P < 0.01$, $^{\#\#\#\#}P < 0.0001$ *vs* the Sham group; $^{*}P < 0.05$, $^{**}P < 0.01$, $^{***}P < 0.001$, $^{****}P < 0.0001$ *vs* the Model group. (E) UMAP plot of 55 839 cells pooled from all groups, showing cells identified based on known cell type markers. (F) UMAP plots of cells from each group. Red arrows indicate the trend of cell number changes in the Model group compared to the Sham group. Black arrows indicate the trend of cell number changes in the treatment group compared to the Model group. Thicker arrows indicate a more pronounced trend. (G) The fraction of the non-cardiomyocyte population relative to all non-cardiomyocytes in each group. (H) Cell numbers of each population in different groups. UMAP, Uniform Manifold Approximation and Projection; NK cells, natural killer cells; DS, Codonopsis Radix extract; HQ, Astragali Radix extract; SQ, Shenqi Fuzheng extract.

ive stress regulation, fibrosis, apoptosis, coagulation, angiogenesis, and ischemia-reperfusion protection [29-40]. Among these representative genes, three (*F3*, *Edn1*, and *Ghr*) were selected for RT-qPCR analysis to validate the reliability of the transcriptomic profiling (Fig. 3D). Notably, *Vegfr1* decreased sharply after AMI and recovered following combination administration compared to monotherapy. *Vegfr1* was expressed in the vascular endothelial cells, suggesting that combination therapy may exert vascular protective and pro-angiogenic effects [41-43].

To prevent the significant biological signals of cardiomyocytes from masking the pathological changes in the non-cardiomyocyte populations [44], such as vascular endothelial cells, scRNA-seq was performed on non-cardiomyocyte-enriched cell populations from the hearts of the Sham, Model, DS, HQ, and SQ (high-dose) groups. As shown in Fig. 3E, 55 839 cells were captured, integrated, clustered, and visualized using UMAP after quality control filtering. The origin of each captured cell was identified (Fig. 3F). Based on the expression of known marker genes, ten non-cardiomyocyte populations were classified, including macrophages and monocytes, endothelial cells, fibroblasts, dendritic cells, glial cells, neutrophils, T cells, B cells, natural killer (NK) cells, and pericytes (Fig. S3A, Table S5)[36, 42, 45-47].

Macrophages and monocytes, endothelial cells, and fibroblasts exhibited the most pronounced changes after AMI (Fig. 3G). On the 3rd day after AMI, the proportion of macrophages and monocytes increased, and fibroblasts also showed an increase to a certain extent, consistent with previous findings [46, 48]. Under homeostatic conditions, endothelial cells constitute the largest population, accounting for more than half of the total cell population. The number of cells in this population declined sharply after AMI, indicating severe endothelial impairment. As shown in Fig. 3H, macrophage and monocyte counts increased after therapy. Fibroblast counts increased progressively with monotherapy and showed a more obvious expansion with combination treatment. Endothelial cell counts did not increase with monotherapy but increased considerably with co-administration. These observations suggest that non-cardiomyocyte populations, especially endothelial cells, may form key cellular targets for mediating the effects of drug therapy.

3.4. SQ (DS and HQ) treatment enhances microvascular endothelial angiogenesis

Endothelial cells are the main components of blood vessels. AMI causes severe damage to endothelial cells, and repair and angiogenesis are essential for managing ischemic injury [35]. Therefore, we performed sub-clustering of these cells and generated UMAP plots (Fig. 4A). The endothelial cells were divided into four subsets (Endo 0–3) with distinct gene signatures. Among them, Endo 0 was predominant in the Sham group (Fig. 4B) and exhibited high expression of hemoglobin genes (*Hbb*, *Hba-a1*, *Hba-a2*), which have been reported to be expressed in endothelial cells and contribute to NO transport and vascular homeostasis (Fig. 4C) [49]. This subset was enriched in the cardiac ventricle morphogenesis pathway, which reflected the basic function of endothelial cells (Fig. S4A). The proportion of Endo 0 was significantly reduced after AMI (Fig. 4B), indicating damage to homeostatic endothelial cells.

Endo 1 exhibited more complex functions. This subpopulation showed increased expression of genes (*Mx1*, *Ifit3*, *Isg20*, etc.) involved in the type I interferon pathway (Fig. 4C, Fig. S4B). This response was triggered by damaged cardiomyocytes in the border zone [50], suggesting that Endo 1 was influenced by cardiomyocyte activity. This subset displayed differential expression of mesenchymal markers (*Postn*, *Col1a1*, *Col1a2*, *Col3a1*, and *Bgn*) (Fig. 4C). Following AMI, endothelial cells transiently acquire a mesenchymal activation (EndMA) state, which may partially support the growth of new blood vessels by promoting endothelial cell migration and invasion [51]. The vasculature development pathway was enriched in this subpopulation (Fig. S4B). Following AMI, new microvessels develop in the border zone, expanding the capillary network with branches and vessels entering the infarct core. Over time, these capillaries grow and are supported by smooth muscle cells [35]. Therefore, this subset represented a post-infarction cluster with superimposed characteristics associated with newborn microvessels in the border zone. Endo 1 showed an increased trend after AMI and was further enriched following treatment, with the highest relative representation observed in the combination group (Fig. 4B).

To investigate whether enhanced microvascular growth may contribute to the synergistic therapeutic effects of DS and HQ, we focused on the vasculature development pathway. Angiogenesis is a sub-pathway of vasculature development within Endo 1 (Fig. 4D). The expression score of the angiogenesis-related gene set was higher in the Model group than in the Sham group. This score increased with DS or HQ treatment and peaked in the SQ group (Fig. 4E), consistent with a stronger pro-angiogenic response. Changes in Endo 1 gene expression across different groups were investigated. The Endo 1 Model group was compared with the Sham, DS, HQ, and SQ groups. DEGs were identified and visualized with volcano plots (Fig. S5A). A total of 153 DEGs were detected in the Model group compared to the Sham group. 379, 287, and 415 DEGs were identified in the DS, HQ, and SQ groups, respectively, compared to the Model group (Fig. 4F). Venn diagrams highlighted DEGs across groups (Fig. 4G). The SQ group showed the largest number of DEGs, suggesting that AMI activates Endo 1 and drives its development, and that DS and HQ together regulate a larger number of DEGs. These DEGs were linked to positive regulation of cell migration, extracellular matrix organization, vasculature development, regulation of endothelial cell migration, and regulation of angiogenesis pathways (Fig. 4H, Fig. S5B). Co-administration enhanced the HUVEC migration rate in wound healing assays (Figs. 4I–4J). The combined treatment resulted in a higher density of microvessels in the border zone compared with monotherapy (Figs. 4K–4L).

Endo 2 expressed numerous chemokine (C-C motif) ligand genes, including *Ccl2*, *Ccl7*, and *Ccl12* (Fig. 4C; Fig. S4C), which can recruit and retain leukocytes at wound sites [52]. Endo 3 was characterized by high expression of cell cycle markers (*Mki67*, *Ccnb2*, and *Cdk1*) (Fig. 4C; Fig. S4D) [42]. However, the numbers of Endo 2 and Endo 3 did not change significantly after drug treatment.

3.5. SQ (DS and HQ) treatment increases the relative abundance and anti-inflammatory activity of reparative macrophages

Monocytes and macrophages are the most abundant non-cardiomyocytes that infiltrate the infarcted myocardium. A second-level clustering analysis was performed on this population to characterize their properties and potential roles. In total, 11 sub-clusters were identified (Fig. 5A).

Monocytes (Mo, subset 9) were first identified based on well-known markers, including *Ly6c* and *Plac8* [46], which were absent or sparsely detected in other populations (Fig. 5B). Next, we analyzed the expression of the signature genes, *Ccr2* and MHC-II (*RT1-Ba*, *RT1-Da*, and *RT1-DMa*), which represent monocyte-derived macrophages and their antigen-presentation potential [53, 54]. Sub-clusters 8 and 10 were classified as MHC^{hi} subsets, primarily contributing to pro-inflammatory events during AMI progression (M1, Fig. 5B) [46]. Marker genes characteristic of both monocytes and monocyte-derived macrophages were detected in subset 7, suggesting that these cells represent an intermediate state between the two populations (MoM1, Fig. 5B). Compared to the Sham group, the proportion of monocytes was reduced and shifted toward pro-inflammatory macrophages in both the Model and treatment groups (Fig. 5C).

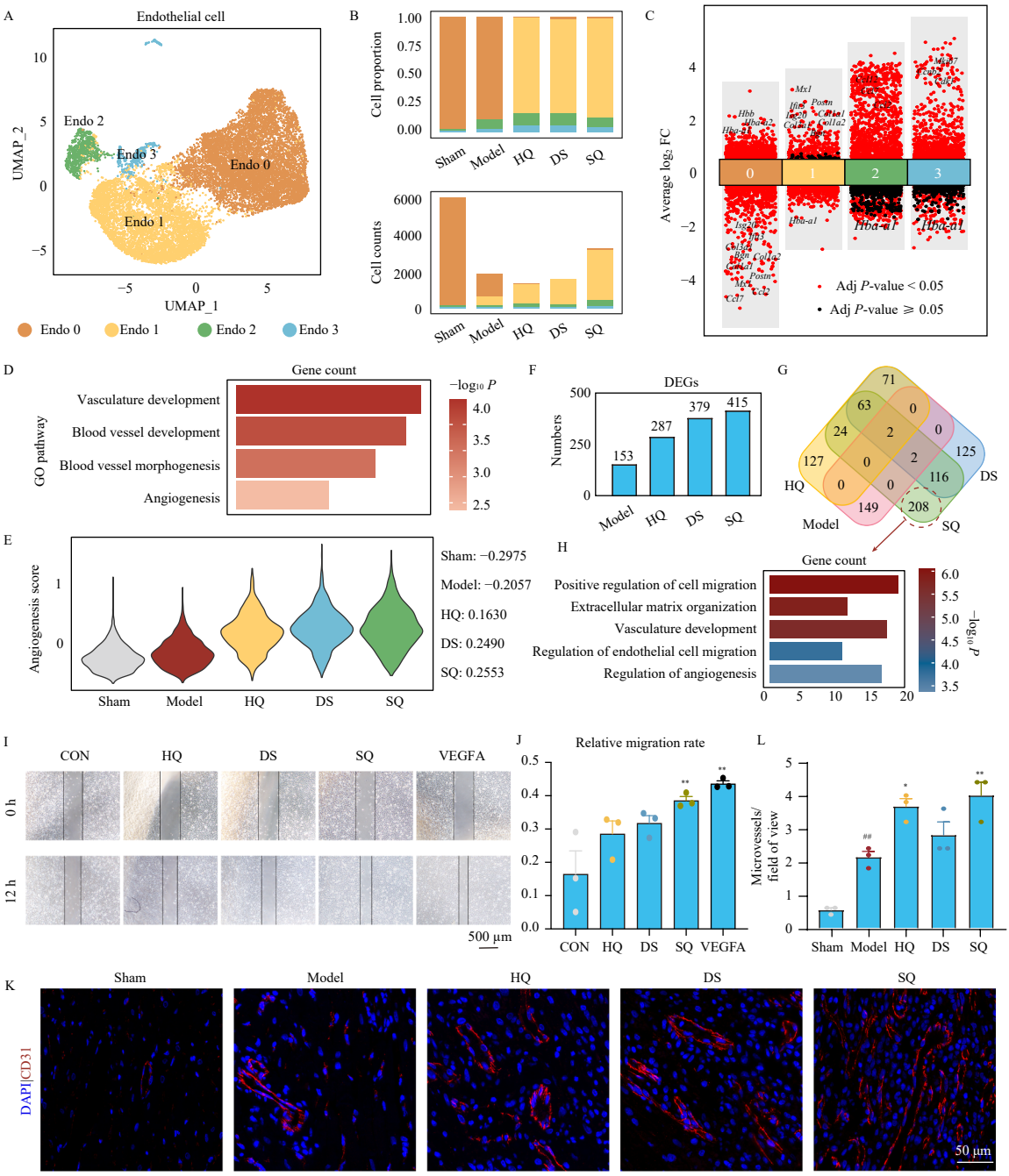


Fig. 4 SQ (DS and HQ) treatment promotes microvascular endothelial angiogenesis. (A) UMAP plot of 14 890 endothelial cells shows 4 merged subsets across all groups. (B) Statistical plots of the proportions and counts of endothelial subsets in different groups. (C) Expression of cell-specific marker genes in each subpopulation. (D) Sub-pathway under the vasculature development pathway. (E) Violin plot of angiogenesis signature gene expression of Endo 1 in different groups. (F) Statistical graph of the number of up-regulated and down-regulated DEGs in Sham and Model, DS and Model, HQ and Model, as well as SQ and Model from Endo 1. (G) Venn plot of DEGs in Sham and Model, DS and Model, HQ and Model, as well as SQ and Model from Endo 1. (H) Pathway enrichment of DEGs expressed only in Endo 1 of the SQ group. (I) Representative images of the cell migration assay. (J) Co-administration promoted the relative cell migration rate in HUVECs, $n = 3$. Data are presented as mean ± SEM. $^{**}P < 0.01$ *vs* the CON group. (K) Representative images of immunofluorescence staining for the vascular endothelial cell marker CD31 (red) in the border zone of different groups. (L) Density statistics of microvessels in the border zone of different groups, $n = 3$. Data are presented as mean ± SEM. $^{\#\#}P < 0.01$ *vs* the Sham group, $^{*}P < 0.05$, $^{**}P < 0.01$ *vs* the Model group. DEGs, differentially expressed genes; UMAP, Uniform Manifold Approximation and Projection; Endo 0, endothelial cells 0; Endo 1, endothelial cells 1; Endo 2, endothelial cells 2; Endo 3, endothelial cells 3; CON, control group; DS, Codonopsis Radix extract; HQ, Astragali Radix extract; SQ, Shenqi Fuzheng extract.

The next subsets exhibited low levels of *Ccr2* and MHC-II expression. Subsets 0 and 5 (Mac 1) displayed high expression levels of complement-related genes, including *C1qa*, *C1qb*, and *C1qc* (Fig. 5B). These were enriched in GO terms associated with immune responses (Fig. 5D; Fig. S7A) and were therefore considered a prototypical macrophage population [46]. Subset 4 (Mac 3) exhibited high expression of *Col3a1*, *Col1a2*, *Col1a1*, and *Bgn* (Fig. 5B) and was related to collagen fibril organization, contributing to tissue fibrosis (Fig. 5D; Fig. S7B). The pro-fibrotic subset becomes prominent 14 days post-AMI and may promote cardiac regeneration [46].

Subsets 1, 2, 3, and 6 (Mac 2) were associated with fatty acid metabolism (Fig. 5D; Fig. S7C). These cells exhibited higher expression of *Trem2*, *Spp1*, *Fabp5*, *Gpnmb*, and *Timp2* (Fig. 5B). These macrophages become predominant during the late phase of AMI and are associated with anti-inflammatory features [45]. Therefore, we characterized Mac 2 as a *Trem2*/*Spp1*/*Gpnmb*/*Fabp5*-enriched reparative macrophage-like subset. In our study, the proportion of Mac 2 increased after AMI and expanded following treatment, reaching the highest levels in the co-administration group (Fig. 5E). Co-administration increased the ratio of Mac 2 counts to *Ccr2*^{hi} macrophage counts and increased the ex-

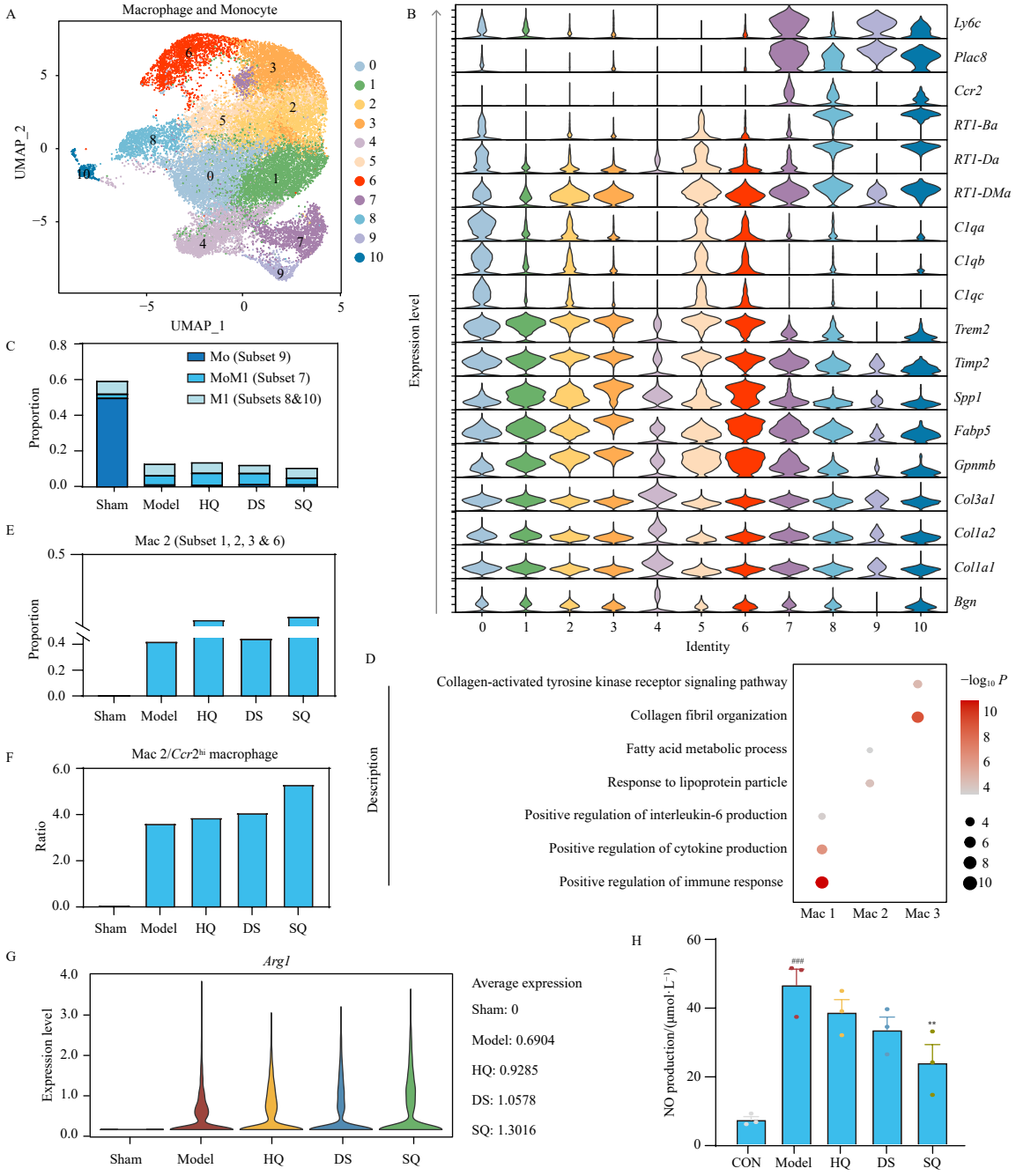


Fig. 5 AMI dataset shows infarction and therapeutic dynamics of monocytes and macrophages. (A) UMAP plot of 25 919 monocytes and macrophages shows 11 subsets merged from all groups. (B) Expression of cell-specific marker genes in all subsets. (C) Statistical plots of the proportion of Mo, MoM1, and M1 subsets in different groups. (D) Dot plot of pathway enrichment levels in Mac 1, Mac 2, and Mac 3. (E) Statistical plots of the proportion of Mac 2 in different groups. (F) The ratio of Mac 2 counts to *Ccr2*^{hi} macrophage counts in all groups. (G) Violin plot of *Arg1* expression of Mac 2 in different groups. (H) NO levels in the BMDM supernatant in the different groups, $n = 3$. Data are presented as mean ± SEM. $^{###}P < 0.001$ *vs* the CON group, $^{**}P < 0.01$ *vs* the Model group. Mo, Monocyte; M1, pro-inflammatory macrophage; MoM1, the subset converted from Monocyte to pro-inflammatory macrophages; Mac 1, Macrophages 1; Mac 2, Macrophages 2; Mac 3, Macrophages 3; UMAP, Uniform Manifold Approximation and Projection; DS, Codonopsis Radix extract; HQ, Astragali Radix extract; SQ, Shenqi Fuzheng extract.

pression level of arginase 1 (*Arg1*, a gene characteristic of M2 macrophages) in Mac 2 (Figs. 5F–5G). In the LPS/IFN-γ-stimulated BMDM model, both HQ and DS reduced NO production, and this inhibitory effect was further amplified after co-administration (Fig. 5H), which was consistent with the enhanced regulation of the *Arg1*-NO pathway following combined HQ and DS treatment.

3.6. SQ (DS and HQ) treatment enhances macrophage–endothelial interactions associated with angiogenesis

Anti-inflammatory macrophages can release high levels of VEGFA, driving angiogenesis [44, 55-57]. Given the enhanced relative dominance of anti-inflammatory macrophages induced by co-administration, we investigated whether macrophage-mediated angiogenesis may contribute to the enhanced effects of combined DS and HQ treatment. The interaction between Endo 1 and Mac 2, as well as their interactions with the VEGFA pathway, was enhanced after AMI. These interactions were further strengthened by either DS or HQ treatment, with the most pronounced enhancement observed in the combination treatment group (Figs. 6A–6B), suggesting that the VEGFA pathway may contribute to the enhanced pro-angiogenic effects of combined DS and HQ treatment. *Vegfa* expression in Mac 2 was higher in the combina-

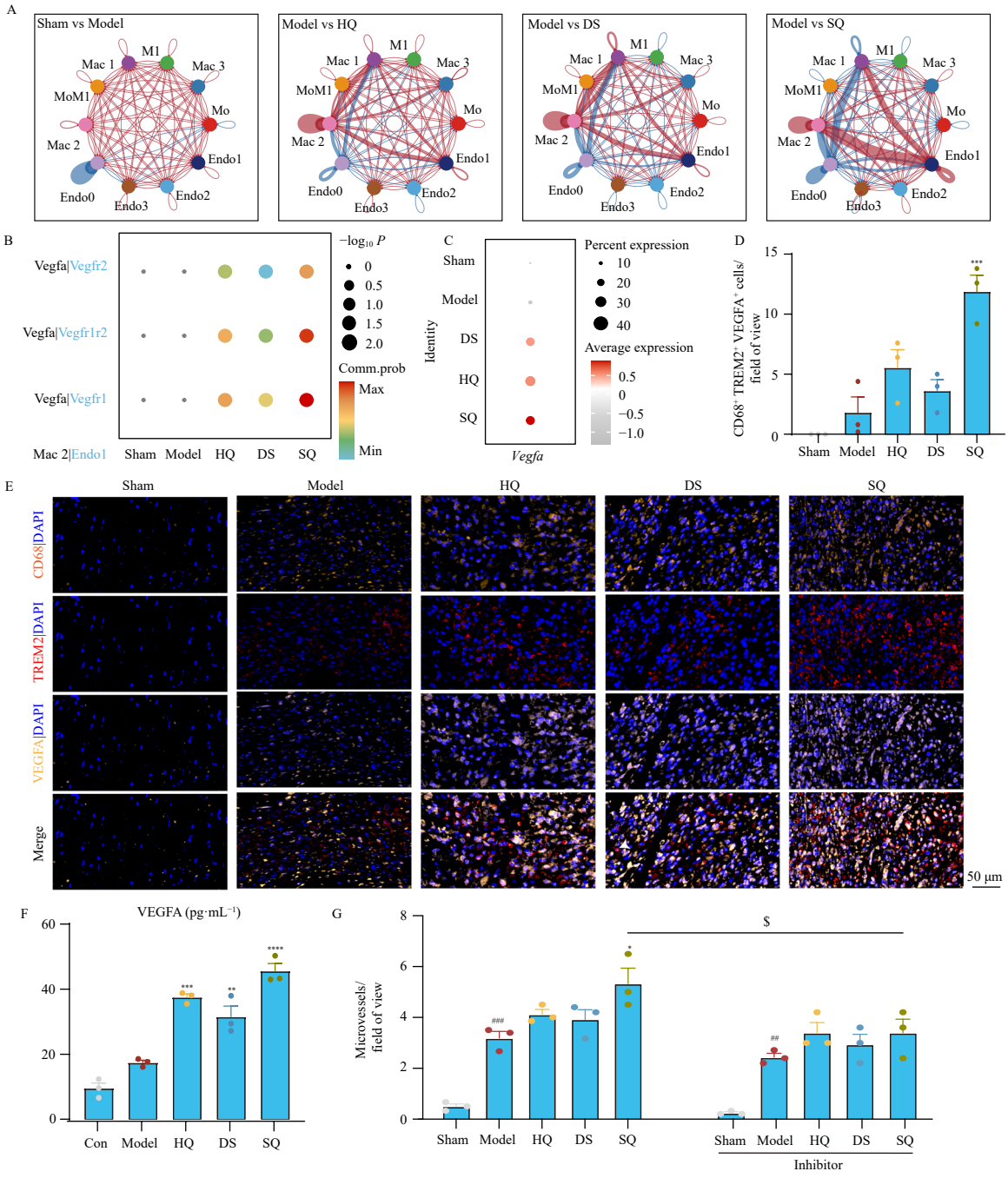


Fig. 6 Combination treatment promotes angiogenesis in endothelial cell subsets and their crosstalk. (A) Overview of CCI between endothelial subsets and monocyte-macrophage subpopulations. Compared to the Sham group, the Model group shows increased (red) or decreased (blue) interactions between monocytes-macrophages and endothelial cells. Similarly, comparisons between the Model and other treatment groups follow the same representation. Thicker lines indicate stronger interactions. (B) Overview of VEGFA-related ligand-receptor interactions between Endo 1 and Mac 2; *P*-values indicated by circle size and scale on the right. The communication probability of interaction is indicated by color. (C) Dot plot showing the expression of *Vegfa* in Mac 2 in each group. (D) Statistical graph of the density of CD68$^+$ TREM2$^+$ VEGFA$^+$ cells in the heart, $n = 3$. Data are presented as mean ± SEM. $^{***}P < 0.001$ *vs* the Model group. (E) Representative images of immunofluorescence staining for the macrophage marker CD68 (orange), signature genes TREM2 (red), and VEGFA (pink) in the hearts of different groups. Nuclei were counterstained with DAPI (blue). White arrows indicate CD68$^+$ TREM2$^+$ VEGFA$^+$ cells in the heart. (F) VEGFA levels in the BMDM supernatant across different groups, $n = 3$. Data are presented as mean ± SEM. $^{**}P < 0.01$, $^{***}P < 0.001$, $^{****}P < 0.0001$ *vs* the Model group. (G) Density statistics of microvessels in the infarct border zone of different groups, $n = 3$. Data are presented as mean ± SEM. $^{\#\#}P < 0.01$, $^{\#\#\#}P < 0.001$ *vs* the Sham group; $^{\$}P < 0.05$ *vs* the Model group; $^{\$}P < 0.05$ *vs* the corresponding inhibitor group. CCI, cell-cell interaction; Mo, Monocyte; M1, pro-inflammatory macrophage; MoM1, the subset converted from Monocyte to pro-inflammatory macrophages; Mac 1, Macrophages 1; Mac 2, Macrophages 2; Mac 3, Macrophages 3; Endo 0, Endothelial cells 0; Endo 1, Endothelial cells 1; Endo 2, Endothelial cells 2; Endo 3, Endothelial cells 3; DS, Codonopsis Radix extract; HQ, Astragali Radix extract; SQ, Shenqi Fuzheng extract.

tion treatment group compared with either DS or HQ treatment alone (Fig. 6C). Immunofluorescence staining showed similar results, with a high density of CD68$^+$ TREM2$^+$ VEGFA$^+$ macrophages present in the SQ group (Figs. 6D–6E). VEGFA levels in the supernatant of LPS/IFN-γ-stimulated BMDMs were significantly elevated following drug treatment, with a more pronounced effect observed under combination therapy (Fig. 6F). This is consistent with the regulatory effects of DS and HQ on VEGFA signaling. Molecular docking analysis suggested that representative compounds from both DS and HQ may bind to distinct sites on VEGFA (Fig. S9). Importantly, pharmacological inhibition of VEGFR signaling by Lenvatinib attenuated microvascular formation and reduced the enhanced pro-angiogenic effect observed under SQ treatment (Fig. 6G, Fig. S10), supporting the involvement of the VEGFA-VEGFR pathway in the vascular protective effects associated with the combined treatment.

3.7. Combination treatment is associated with the expansion of proliferative fibroblasts during early cardiac repair

Cardiac fibroblasts are essential for maintaining cardiac structure and mediating post-infarction repair [58, 59]. The fibroblasts clustered into nine subpopulations (Fig. S11A). Subclusters 3, 7, and 8 expressed resident fibroblast markers, including *Lpl*, *Pdgfra*, and *Tcf21* [47, 60], and were predominantly enriched in the Sham group (Figs. S11B–S11C). In contrast, subsets 4 and 6 exhibited elevated expression of inflammatory genes such as *Il1b*, *Ccl3*, and *Ccl4*, indicating an inflammatory fibroblast state [43]. Subsets 0, 1, and 5 expressed genes associated with fibroblast activation and scar repair, including *Acta2*, *Postn*, *Fn1*, *Lox*, and *Cthrc1* (Fig. S11B). *Acta2* is a myofibroblast marker [48], *Postn*, *Fn1*, and *Lox* are associated with extracellular matrix (ECM) composition and modification [60], *Cthrc1* regulates the scar-healing process and prevents ventricular rupture [13]. These subsets may represent reparative fibroblasts described in a previous study [41].

In addition, sub-cluster 2 predominantly expressed proliferative genes, including *Cdk1*, *Ccnb2*, and *Mki67* [42]. *Mki67*^{hi} fibroblasts contribute to the generation of reparative fibroblasts following AMI [41]. This proliferative fibroblast subpopulation emerged after infarction and showed a trend toward further expansion following combination treatment (Fig. S11C), suggesting that co-administration promotes fibroblast proliferation during cardiac repair.

4. Discussion

The SQ formulation has demonstrated significant protective effects against myocardial ischemia [2]; however, the mechanisms underlying the combined use of DS and HQ in this formulation remain unclear. Current studies on AMI emphasize the critical role of non-cardiomyocytes in mitigating cardiomyocyte loss and dysfunction in the infarct border zone, particularly immune cells, endothelial cells, and fibroblasts. After AMI, microvascular endothelial cells play a key role in rapidly establishing a dense capillary network in the ischemic heart, a process mediated by specific macrophage subsets. These macrophages not only contribute to the resolution of inflammation but also support angiogenesis, thereby promoting vascular repair [55, 56]. Additionally, the formation of capillaries provides a conduit for inflammatory cell infiltration and supports gas exchange, nutrient delivery, and waste removal, meeting the elevated metabolic demands of the injured tissue [35]. Meanwhile, fibroblasts provide structural support for angiogenesis by producing and depositing ECM components, facilitating vessel stability and maturation [59].

In macrophages, we identified a *Trem2*/*Spp1*/*Gpnmb*/*Fabp5*-enriched reparative macrophage-like subset (Mac 2) with anti-inflammatory and pro-angiogenic features. This subset participates in inflammation resolution and indirectly supports microvascular formation through enhanced VEGFA-related signaling. Under combined treatment, *Arg1* expression and VEGFA secretion were elevated in this macrophage subset, strengthening the signaling through endothelial VEGFR and linking immune regulation with vascular repair. Notably, the *Arg1*-NO and VEGF pathways in Mac 2 exhibited more significant changes under combination therapy, but the expression of marker genes defining this subset did not follow similar trends (Fig. S12). This suggests that the synergistic effect may not primarily involve direct regulation of these marker genes but may instead be associated with modulation of metabolic and functional pathways within Mac 2. Furthermore, while HQ is less potent than DS in inhibiting NO production, it more strongly upregulates VEGFA. The precise mechanisms underlying these differences require further investigation.

Fibroblasts are typically associated with scar formation during wound healing and the maintenance of structural integrity [41]. Although the combined treatment also showed a trend toward promoting proliferation, no significant enhancement was observed compared to the monotherapy groups. This may be attributed to the early time point assessed (3 days post-AMI), where the effects may not yet have fully manifested. Changes in these cell populations are often more evident one week after AMI [61, 62].

Moreover, previous studies have shown that the chemical constituents of DS and HQ regulate multiple biological pathways, including myocardial differentiation, inflammation, endothelial protection, and angiogenesis, which are closely associated with AMI therapy [63-66]. In the present study, molecular docking analysis indicated that representative compounds from DS and HQ could bind to distinct regions of VEGFA, providing a potential structural basis for their efficacy.

However, this study has some limitations. First, this study primarily focused on the synergistic mechanisms of the SQ formulation, and comparisons with positive controls were performed in our previous work; therefore, a positive control group was not included in the present study [2]. Future investigations may incorporate a positive control group based on the synergistic mechanisms identified here. Second, this study examined an early time point after AMI to capture the acute inflammatory response and initial repair signals. Given that myocardial repair is a dynamic process, the strength and duration of the synergistic effects of DS and HQ may vary during subsequent repair and remodeling stages, which warrants further investigation at multiple time points. Third, although the BMDM experiments partially reflected the transcriptional characteristics of the Mac 2 population through representative marker genes, the *in vitro* BMDM system could not fully recapitulate the complex microenvironment and dynamic macrophage state transitions observed *in vivo* after AMI. Future studies incorporating additional *in vivo* validation strategies may further clarify the relationship between the Mac 2 population and the observed synergistic therapeutic effects.

5. Conclusion

DS and HQ in the SQ formula exhibit a synergistic therapeutic effect in AMI. This study integrates bulk and single-cell transcriptomic analyses to elucidate the synergistic mechanisms of DS and HQ in the treatment of AMI. Compared to monotherapy, combination treatment not only directly promoted endothelial microvascular formation but also enhanced the anti-inflammatory and pro-angiogenic abilities of a type of reparative macrophage subset, thereby indirectly promoting microvascular angiogenesis through macrophage-endothelial crosstalk. These findings provide scientific evidence for the application of TCM in AMI.

Funding

This work was supported by the Zhejiang Provincial Natural Science Foundation of China (No. LD25H280002), 'Pioneer' and 'Leading Goose' R&D Program of Zhejiang Province (No. 2024C03106), the National Natural Science Foundation of China (No. 82204772), and Starlit South Lake Leading Elite Program (No. 2023A303005).

Supporting information

Supporting information for this work can be obtained by contacting the corresponding authors *via* E-mail.

Declaration of competing interest

The authors declare that they have no competing interests.

Availability of data and materials

The datasets used and/or analyzed during the current study can be requested by sending E-mail to the corresponding authors.

References

1 Wang ML, Zhu BJ, Gao M, et al. Identification of chemical constituents and blood-absorbed components of Shenqi Fuzheng extract based on UPLC-Triple-TOF/MS technology. *Future Integr Med*. 2024;3:222-238. https://doi.org/10.14218/fim.2024.00037.

2 Liao J, Hao C, Huang WH, et al. Network pharmacology study reveals energy metabolism and apoptosis pathways-mediated cardioprotective effects of Shenqi Fuzheng. *J Ethnopharmacol*. 2018;227:155-165. https://doi.org/10.1016/j.jep.2018.08.029.

3 Du J, Cheng BCY, Fu X, et al. *In vitro* assays suggest Shenqi Fuzheng Injection has the potential to alter melanoma immune microenvironment. *J Ethnopharmacol*. 2016;194:15-19. https://doi.org/10.1016/j.jep.2016.08.038.

4 Ma YR, Bai BF, Liu D, et al. Shenqi Fuzheng Injection reduces cisplatin-induced kidney injury *via* cGAS/STING signaling pathway in breast cancer mice model. *Breast Cancer (Dove Med Press)*. 2024;16:451-469. https://doi.org/10.2147/bctt.S475860.

5 Guo W, Liu S, Xia H, et al. Shenqi Fuzheng injection facilitates skeletal muscle mitophagy mediated by the ubiquitination of HIF-1α to ameliorate cancer-associated fatigue. *J Cell Mol Med*. 2024;28:e18455. https://doi.org/10.1111/jcmm.18455.

6 Xiao D, Zhang HZ, Zuo XH, et al. Observation on the efficacy of Shenqi Fuzheng Injection in treating senile heart failure after acute myocardial infarction. *Chin J Integr Med Cardio Cerebrovsc Dis*. 2016;14:1061-1063. https://doi.org/10.3969/j.issn.1672-1349.2016.10.002.

7 Yun ML. Clinic observation of 55 cases with chronic heart failure treated by shenqi fuzheng injection. *Nat Sci J Hainan Univ*. 2006;24:371-373. https://doi.org/1004-1729(2006)04-0371-03.

8 liu P, Xu XY, Li M. Effect of shenqi fuzheng injection on peripheral blood ANGII, ET-1 levels and clinical curative effect in patients with congestive heart failure. *Chin J Biochem Pharm*. 2015;35:81-83. https://doi.org/1005-1678(2015)12-0081-03.

9 Wang L, Ye BH, Wang DX, et al. Effects of Shenqi Fuzheng Injection on plasma N terminal pro-brain natriuretic peptide in patients with chronic heart failure. *Pract J Cardiac Cereb Pneum Vasc Dis*. 2011;19:1774-1775. https://doi.org/1008-5971(2011)10-1774-02.

10 Tsao CW, Aday AW, Almarzooq ZI, et al. Heart disease and stroke statistics—2023 update: a report from the American heart association. *Circulation*. 2023;147:e622. https://doi.org/10.1161/cir.0000000000001123.

11 Zhou MG, Wang HD, Zeng XY, et al. Mortality, morbidity, and risk factors in China and its provinces, 1990–2017: a systematic analysis for the Global Burden of Disease Study 2017. *Lancet*. 2019;394:1145-1158. https://doi.org/10.1016/s0140-6736(19)30427-1.

12 Wang XW, Guo ZK, Ding ZF, et al. Inflammation, autophagy, and apoptosis after myocardial infarction. *J Am Heart Assoc*. 2018;7:e008024. https://doi.org/10.1161/jaha.117.008024.

13 Ruiz-Villalba A, Romero JP, Hernández SC, et al. Single-cell RNA sequencing analysis reveals a crucial role for *CTHRC1* (Collagen Triple Helix Repeat Containing 1) cardiac fibroblasts after myocardial infarction. *Circulation*. 2020;142:1831-1847. https://doi.org/10.1161/circulationaha.119.044557.

14 Yu Q, Guo DW, Peng JN, et al. Prevalence and adverse outcomes of frailty in older patients with acute myocardial infarction after percutaneous coronary interventions: a systematic review and meta-analysis. *Clin Cardiol*. 2022;46:5-12. https://doi.org/10.1002/clc.23929.

15 Takura T, Komuro I, Ono M. Trends in the cost-effectiveness level of percutaneous coronary intervention: macro socioeconomic analysis and health technology assessment. *J Cardiol*. 2023;81:356-363. https://doi.org/10.1016/j.jjcc.2022.09.011.

16 Al Said S, Kaier K, Sumaya W, et al. Non-vitamin-K-antagonist oral anticoagulants (NOACs) after acute myocardial infarction: a network meta-analysis. *Cochrane Database Syst Rev*. 2024;1:e014678. https://doi.org/10.1002/14651858.CD014678.pub2.

17 Jiang BP, Si JY, Luo HM, et al. Single-cell omics reveal the mechanisms of traditional Chinese medicines. *Phytomedicine*. 2025;147:157204. https://doi.org/10.1016/j.phymed.2025.157204.

18 Gu YC, Wang GJ, Pan GY, et al. Transport and bioavailability studies of astragaloside IV, an active ingredient in Radix Astragali. *Basic Clin Pharmacol Toxicol*. 2004;95:295-298. https://doi.org/10.1111/j.1742-7843.2004.t01-1-pto950508.x.

19 Du Y, Zhang Q, Chen G, et al. Pharmacokinetics of Astragaloside IV in rats by liquid chromatography coupled with tandem mass spectrometry. *Eur J Drug Metab Pharmacokinet*. 2005;30:269-273. https://doi.org/10.1007/BF03190631.

20 Matsui J, Yamamoto Y, Funahashi Y, et al. E7080, a novel inhibitor that targets multiple kinases, has potent antitumor activities against stem cell factor producing human small cell lung cancer H146, based on angiogenesis inhibition. *Int J Cancer*. 2008;122:664-671. https://doi.org/10.1002/ijc.23131.

21 Foucquier J, Guedj M. Analysis of drug combinations: current methodological landscape. *Pharmacol Res Perspect*. 2015;7:e00549. https://doi.org/10.1002/prp2.149.

22 Vlot AHC, Aniceto N, Menden MP, et al. Applying synergy metrics to combination screening data: agreements, disagreements and pitfalls. *Drug Discov Today*. 2019;24:2286-2298. https://doi.org/10.1016/j.drudis.2019.09.002.

23 Wu LH, Li X, Yang JH, et al. CHD@ZJU: a knowledgebase providing network-based research platform on coronary heart disease. *Database (Oxford)*. 2013;2013:bat047. https://doi.org/10.1093/database/bat047.

24 Wu LH, Wang Y, Li Z, et al. Identifying roles of Jun-Chen-Zuo-Shi component herbs of QiShenYiQi formula in treating acute myocardial ischemia by network pharmacology. *Chin Med*. 2014;9:24. https://doi.org/10.1186/1749-8546-9-24.

25 Xu XJ, Long JB, Jin KY, et al. Danshen-Chuanxiongqin Injection attenuates cerebral ischemic stroke by inhibiting neuroinflammation *via* the TLR2/TLR4-MyD88-NF-κB Pathway in tMCAO mice. *Chin J Nat Med*. 2021;19:772-783. https://doi.org/10.1016/s1875-5364(21)60083-3.

26 Hao Y, Stuart T, Kowalski MH, et al. Dictionary learning for integrative, multimodal and scalable single-cell analysis. *Nat Biotechnol*. 2023;42:293-304. https://doi.org/10.1038/s41587-023-01767-y.

27 Han C, Shi CP, Liu LM, et al. Majorbio Cloud 2024: update single-cell and multiomics workflows. *iMeta*. 2024;3:e217. https://doi.org/10.1002/imt2.217.

28 Jin SQ, Guerrero-Juarez CF, Zhang LH, et al. Inference and analysis of cell-cell communication using CellChat. *Nat Commun*. 2021;12:1088. https://doi.org/10.1038/s41467-021-21246-9.

29 Hathaway CK, Grant R, Hagaman JR, et al. Endothelin-1 critically influences cardiac function *via* superoxide-MMP9 cascade. *Proc Natl Acad Sci USA*. 2015;112:5141-5146. https://doi.org/10.1073/pnas.1504557112.

30 Clancy RM, Markham AJ, Jackson T, et al. Cardiac fibroblast transcriptome analyses support a role for interferogenic, profibrotic, and inflammatory genes in anti-SSA/Ro-associated congenital heart block. *Am J Physiol Heart Circ Physiol*. 2017;313:631-640. https://doi.org/10.1152/ajpheart.00256.2017.

31 Zheng M, Liu ZY, Liu NN, et al. The effect of Wenxin Keli on the mRNA expression profile of rabbits with myocardial infarction. *Evid Based Compl Alt*. 2016;2016:2352614. https://doi.org/10.1155/2016/2352614.

32 Wang YH, Xian HM. Identifying genes related to acute myocardial infarction based on network control capability. *Genes (Basel)*. 2022;13:1238. https://doi.org/10.3390/genes13071238.

33 Li S, Tao B, Wan JJ, et al. A humanized monoclonal antibody targeting an ectonucleotidase rescues cardiac metabolism and heart function after myocardial infarction. *Cell Rep Med*. 2024;5:101795. https://doi.org/10.1016/j.xcrm.2024.101795.

34 Yang SY, Pei LY, Huang ZJ, et al. Inhibition of tartrate-resistant acid phosphatase 5 can prevent cardiac fibrosis after myocardial infarction. *Mol Med*. 2024;30:89. https://doi.org/10.1186/s10020-024-00856-1.

35 Wu XK, Reboll MR, Korf-Klingebiel M, et al. Angiogenesis after acute myocardial infarction. *Cardiovasc Res*. 2021;117:1257-1273. https://doi.org/10.1093/cvr/cvaa287.

36 Gladka MM, Molenaar B, de Ruiter H, et al. Single-cell sequencing of the healthy and diseased heart reveals cytoskeleton-associated protein 4 as a new modulator of fibroblasts activation. *Circulation*. 2018;138:166-180. https://doi.org/10.1161/CIRCULATIONAHA.117.030742.

37 Kim JO, Park JH, Kim T, et al. A novel system-level approach using RNA-sequencing data identifies miR-30-5p and miR-142a-5p as key regulators of apoptosis in myocardial infarction. *Sci Rep*. 2018;8:14638. https://doi.org/10.1038/s41598-018-33020-x.

38 Grover SP, Mackman N. Tissue factor in atherosclerosis and atherothrombosis. *Atherosclerosis*. 2020;307:80-86. https://doi.org/10.1016/j.atherosclerosis.2020.06.003.

39 Mao XL, Xu H, Liu XL, et al. Proteomics of urinary exosomes for discovering novel non-invasive biomarkers of acute myocardial infarction patients. *Int J Biol Macromol*. 2025;302:140427. https://doi.org/10.1016/j.ijbiomac.2025.140427.

40 Budas GR, Churchill EN, Disatnik MH, et al. Mitochondrial import of PKCepsilon is mediated by HSP90: a role in cardioprotection from ischaemia and reperfusion injury. *Cardiovasc Res*. 2010;88:83-92. https://doi.org/10.1093/cvr/cvq154.

41 Ke D, Cao MZ, Ni J, et al. Macrophage and fibroblast trajectory inference and crosstalk analysis during myocardial infarction using integrated single-cell transcriptomic datasets. *J Transl Med*. 2024;22:560. https://doi.org/10.1186/s12967-024-05353-x.

42 Farbehi N, Patrick R, Dorison A, et al. Single-cell expression profiling reveals dynamic flux of cardiac stromal, vascular and immune cells in health and injury. *eLife*. 2019;8:e43882. https://doi.org/10.7554/eLife.43882.

43 Tallquist MD. Cardiac fibroblast diversity. *Annu Rev Physiol*. 2020;82:63-78. https://doi.org/10.1146/annurev-physiol-021119-034527.

44 Yap J, Irei J, Lozano-Gerona J, et al. Macrophages in cardiac remodelling after myocardial infarction. *Nat Rev Cardiol*. 2023;20:373-385. https://doi.org/10.1038/s41569-022-00823-5.

45 Jung SH, Hwang BH, Shin S, et al. Spatiotemporal dynamics of macrophage heterogeneity and a potential function of $Trem2^{hi}$ macrophages in infarcted hearts. *Nat Commun*. 2022;13:4580. https://doi.org/10.1038/s41467-022-32284-2.

46 Jin KY, Gao S, Yang PH, et al. Single-cell RNA sequencing reveals the temporal diversity and dynamics of cardiac immunity after myocardial infarction. *Small Methods*. 2022;6:e2100752. https://doi.org/10.1002/smtd.202100752.

47 Tani H, Sadahiro T, Yamada Y, et al. Direct reprogramming improves cardiac function and reverses fibrosis in chronic myocardial infarction. *Circulation*. 2023;147:223-238. https://doi.org/10.1161/CIRCULATIONAHA.121.058655.

48 Ivey MJ, Kuwabara JT, Pai JT, et al. Resident fibroblast expansion during cardiac growth and remodeling. *J Mol Cell Cardiol*. 2018;114:161-174. https://doi.org/10.1016/j.yjmcc.2017.11.012.

49 Straub AC, Lohman AW, Billaud M, et al. Endothelial cell expression of haemoglobin alpha regulates nitric oxide signalling. *Nature*. 2012;491:473-477. https://doi.org/10.1038/nature11626.

50 Ninh VK, Calcagno DM, Yu JD, et al. Spatially clustered type I interferon responses at injury borderzones. *Nature*. 2024;633:174-181. https://doi.org/10.1038/s41586-024-07806-1.

51 Tombor LS, John D, Glaser SF, et al. Single cell sequencing reveals endothelial plasticity with transient mesenchymal activation after myocardial infarction. *Nat Commun*. 2021;12:681. https://doi.org/10.1038/s41467-021-20905-1.

52 Martin P, Leibovich SJ. Inflammatory cells during wound repair: the good, the bad and the ugly. *Trends Cell Biol*. 2005;15:599-607. https://doi.org/10.1016/j.tcb.2005.09.002.

53 Epelman S, Lavine KJ, Beaudin AE, et al. Embryonic and adult-derived resident cardiac macrophages are maintained through distinct mechanisms at steady state and during inflammation. *Immunity*. 2014;40:91-104. https://doi.org/10.1016/j.immuni.2013.11.019.

54 Bajpai G, Bredemeyer A, Li WJ, et al. Tissue resident CCR2- and CCR2+ cardiac macrophages differentially orchestrate monocyte recruitment and fate specification following myocardial injury. *Circ Res*. 2019;124:263-278. https://doi.org/10.1161/CIRCRESAHA.118.314028.

55 Das A, Sinha M, Datta S, et al. Monocyte and macrophage plasticity in tissue repair and regeneration. *Am J Pathol*. 2015;185:2596-2606. https://doi.org/10.1016/j.ajpath.2015.06.001.

56 Ferraro B, Leoni G, Hinkel R, et al. Pro-angiogenic macrophage phenotype to promote myocardial repair. *J Am Coll Cardiol*. 2019;73:2990-3002. https://doi.org/10.1016/j.jacc.2019.03.503.

57 Lu XY, Yao JK, Li CX, et al. Shexiang Tongxin Dropping Pills promote macrophage polarization-induced angiogenesis against coronary microvascular dysfunction *via* PI3K/Akt/mTORC1 pathway. *Front Pharmacol*. 2022;13:840521. https://doi.org/10.3389/fphar.2022.840521.

58 Tallquist MD, Molkentin JD. Redefining the identity of cardiac fibroblasts. *Nat Rev Cardiol*. 2017;14:484-491. https://doi.org/10.1038/nrcardio.2017.57.

59 Shinde AV, Frangogiannis NG. Mechanisms of fibroblast activation in the remodeling myocardium. *Curr Pathobiol Rep*. 2017;5:145-152. https://doi.org/10.1007/s40139-017-0132-z.

60 Fu X, Khalil H, Kanisicak O, et al. Specialized fibroblast differentiated states underlie scar formation in the infarcted mouse heart. *J Clin Invest*. 2018;128:2127-2143. https://doi.org/10.1172/JCI98215.

61 Sun Y, Weber KT. Infarct scar: a dynamic tissue. *Cardiovasc Res*. 2000;46:250-256. https://doi.org/10.1016/s0008-6363(00)00032-8.

62 Yin YF, Tan MY, Han LH, et al. The hippo kinases MST1/2 in cardiovascular and metabolic diseases: a promising therapeutic target option for pharmacotherapy. *Acta Pharm Sin B*. 2023;13:1956-1975. https://doi.org/10.1016/j.apsb.2023.01.015.

63 Cheng SY, Zhang XX, Feng Q, et al. Astragaloside IV exerts angiogenesis and cardioprotection after myocardial infarction *via* regulating PTEN/PI3K/Akt signaling pathway. *Life Sci*. 2019;227:82-93. https://doi.org/10.1016/j.lfs.2019.04.040.

64 Pan L, Zhang XF, Wei WS, et al. The cardiovascular protective effect and mechanism of calycosin and its derivatives. *Chin J Nat Med*. 2020;18:907-915. https://doi.org/10.1016/S1875-5364(20)60034-6.

65 Wang JN, Kan CD, Lee LT, et al. Herbal extract from *Codonopsis pilosula* (Franch.) Nannf. enhances cardiogenic differentiation and improves the function of infarcted rat hearts. *Life (Basel)*. 2021;11:422. https://doi.org/10.3390/life11050422.

66 Chen XY, Shao R, Wang Y. Multi-layered effects of Codonopsis Radix on the immune system. *Acupunct Herb Med*. 2024;4:405-419. https://doi.org/10.1097/hm9.0000000000000130.